Explicit Finite Volume Modeling of Aircraft Anti-Icing and De-Icing

Ouahid Harireche,* Patrick Verdin,† Chris P. Thompson,‡ and David W. Hammond§
Cranfield University,
Cranfield, Bedfordshire MK43 0AL, United Kingdom

In this paper, a runback water and ice prediction model is extended to anti-icing and thermal de-icing situations. The resulting coupled equations that govern thin-film flow, ice accretion, and heat conduction in the multilayered system substrate–ice–water are solved using an explicit finite volume approach. The procedure is implemented in the three-dimensional icing code ICECREMO2, and both structured and unstructured grids can be considered. Numerical results are presented to compare the present code simulations to some data provided by other ice prediction codes and to show the capabilities of the present numerical tool.

Nomenclature

$\mathbf{A}$	=	shear stress at the surface of water film
A	=	cell boundary
A_Q^s, A_Q^i	=	boundary of substrate and ice, respectively, where heat flux is prescribed
b	=	ice thickness
c_s, c_i, c_w	=	specific heat of substrate, ice, and water, respectively
D^{wa}/Dt	=	convective derivative following the motion of water–air interface
D^{wi}/Dt	=	convective derivative following the motion of water–ice interface
$\mathbf{e}_x, \mathbf{e}_y, \mathbf{e}_z$	=	unit vector in the rectangular coordinate system
g_x, g_y, g_z	=	components of gravity
h	=	water film thickness
h_c	=	heat transfer coefficient between substrate and de-icing (or anti-icing) system
J_w	=	mass flux of impinging water droplets
k_s, k_i, k_w	=	heat conductivity of substrate, ice, and water, respectively
L_e	=	latent heat of evaporation
L_f	=	latent heat of freezing
$\dot{m}^I$	=	rate of mass supply by impinging droplets
N_I	=	number of interfaces in a multilayered substrate
$\mathbf{n}$	=	outward unit normal to the boundary of the substrate finite volume
$\mathbf{n}^{wa}$	=	outward unit normal to water–air interface
$\mathbf{n}^{wi}$	=	outward unit normal to water–ice interface
p	=	water pressure
Q_{cond}	=	heat flux due to conduction in the substrate
Q_c	=	heat loss due to convection
Q_d	=	heat loss due to cooling by supercooled droplets
Q_e	=	evaporative heat flux
Q_H	=	power of de-icing heater
Q_k	=	kinetic heat supply
Q_l	=	latent heat supply by impinging droplets
Q_{melt}	=	energy required to melt the ice
$\mathbf{Q}_s, \mathbf{Q}_i, \mathbf{Q}_w$	=	heat flux in the substrate, ice, and water, respectively
$\mathbf{Q}_{sF}, \mathbf{Q}_{iF}, \mathbf{Q}_{wF}$	=	heat flux at the face centroid in substrate, ice, and water, respectively
Q_{subl}	=	heat loss due to ice sublimation
$\mathbf{Q}_w$	=	water flux
Q_0	=	heat supply from de-icing (or anti-icing) system
Q^*	=	heat flux at the surface of substrate
Re	=	Reynolds number
T_{ij}	=	components of stress tensor in the water film, $i, j = 1, \ldots, 3$
T_s, T_i, T_w	=	temperature in the substrate, ice, and water, respectively
T_{sc}, T_{ic}, T_{wc}	=	temperature at the cell centroid in substrate, ice, and water, respectively
T_0	=	air temperature in the de-icing (or anti-icing) system
T^*	=	temperature at the surface of substrate
t	=	time
$\mathbf{t}_x^{wa}, \mathbf{t}_y^{wa}$	=	unit tangents on water–air interface
$\mathbf{t}_x^{wi}, \mathbf{t}_y^{wi}$	=	unit tangents on water–ice interface
u, v, w	=	components of the velocity field in the water film
u_i	=	ith component of the velocity field in the water film, $i = 1, \ldots, 3$
$\mathbf{u}^{wa}$	=	normal velocity of water–air interface
$\mathbf{u}^{wi}$	=	normal velocity of water–ice interface
W	=	freestream velocity
x, y, z	=	rectangular coordinates
x_i	=	ith rectangular coordinate, $i = 1, \ldots, 3$
$\mathbf{x}_F$	=	coordinate vector of the face centroid
z_I	=	z coordinate of interface I in a multilayered substrate
β	=	collection efficiency
γ	=	constant in surface tension relationship to temperature

*Senior Lecturer, School of Engineering, Applied Mathematics and Computing Group; currently University of Greenwich, School of Engineering, Department of Civil Engineering, Chatham Maritime, Kent, ME4 4TB, United Kingdom.

†Lecturer, School of Engineering, Applied Mathematics and Computing Group.

‡Professor, School of Engineering, Applied Mathematics and Computing Group.

§Senior Lecturer, School of Engineering, Applied Mathematics and Computing Group.

ΔA^s, ΔA^i	=	boundary of cell volume in the substrate and ice, respectively
Δt	=	time step
ΔV	=	cell volume
ΔV^s, ΔV^i	=	cell volume in the substrate and ice, respectively
δ_{ij}	=	Kronecker symbol, $i, j = 1, \ldots, 3$
κ	=	mean curvature of water film surface
μ_w	=	water viscosity
ρ_a	=	atmospheric pressure
ρ_v	=	vapor mass density
ρ_w, ρ_i, ρ_A	=	mass density of water, ice, and water droplets in the air, respectively
σ	=	surface tension
σ_0	=	maximum surface tension
ψ^{wa}	=	nonmaterial surface coinciding with water–air interface
ψ^{wi}	=	nonmaterial surface coinciding with water–ice interface
∇	=	gradient operator

I. Introduction

AIRCRAFT icing is a well-known phenomenon that usually occurs in-flight when supercooled droplets that may exist in clouds are intercepted by aircraft wings, engine inlets, and other aircraft components. At combinations of lower temperatures and low-liquid-water content, the impinging supercooled water droplets tend to freeze very rapidly upon impact on the metal surface. This ice is known as rime. At milder temperatures and higher liquid water contents, only one part of the impinging droplets freezes immediately upon contact. The other part remains liquid and may flow and freeze in downstream regions, due to the combined action of air shear and gravity. In this situation, the surface temperature is influenced by the release of latent heat from the freezing of the impinging droplets and glaze ice appears.

Ice accretion is known to cause both weight and drag increase, while reducing the lift, and globally results in a degradation of the aircraft aerodynamic performance and handling. Ice protection systems are therefore required.

De-icing equipment is used to periodically remove accreted ice which has built up to moderate thickness. This is achieved with electrothermal ice protection systems by activating heaters that are embedded in the substrate composite skin, which cause the ice to shed under the combined action of the thermal weakening of adhesive forces, possible melting, and aerodynamic forces. Anti-icing systems are more suitable for aircraft components upstream of aircraft components that might be subject to damage under the effect of ice shedding. This is, for instance, the case of engine inlets, where ice shedding can cause damage of fan blades. It is therefore required to continuously activate an anti-icing system to maintain the surface temperature above freezing and keep the surface free of ice.

The first anti-icing calculations, introduced by Hardy [1], were based on a simplified model that treats the water layer and the metal substrate as a single medium for which a heat balance is performed. Heat loss by convection, evaporation, and sensible and kinetic heat contributions from impinging water droplets are all considered in this heat balance. A more accurate model has been proposed by Al-Khalil et al. [2], which considers separately the water film and the substrate. An energy balance is performed for each medium and a mass balance is performed for the water film. A simple phase-change prediction is also used to identify the region where water starts to freeze. More recently, Al-Khalil et al. [3] have proposed an anti-icing model that takes into account the formation of rivulets. This was particularly motivated by the need to consider the fraction of the surface that is wetted by the runback water, which is referred to as the wetness factor. Indeed, studies by Hansman et al. [4,5] have shown that, during glaze ice accretion, distinct zones of surface water behavior are observed: a zone with a uniform water film in the stagnation region, where the wetness factor has a value of unity, and a rough zone, where the water film breaks into beads and rivulets and where

the wetness factor drops to values on the order of 0.3. A detailed literature review on aircraft anti-icing and de-icing techniques and modeling can be found in [6].

The main purpose of the present paper is to extend the model proposed by Myers et al. [7,8] for runback water flow/ice accretion to consider anti-icing and de-icing situations. The model has been implemented in the 3-D ice prediction code ICECREMO2, which performs explicit transient ice calculations using both structured and unstructured grids. The present work has been mainly motivated by the need to extend ICECREMO capabilities to model both anti-icing and de-icing equipment. The governing equations for the modeling of runback water flow/ice accretion in the presence of heating sources are presented in Sec. II. Water film flow, ice accretion, and heat conduction problems are presented. These problems are coupled and the resulting system of equations, which involves governing equations, boundary and interface conditions, needs to be solved simultaneously. However, the procedure is much simpler when an explicit approach is used, as this allows one to deal separately with film flow/ice accretion and heat conduction problems. The present work adopts an explicit solution procedure for both anti-icing and de-icing problems. In the anti-icing case, ice accretion is ignored and both water flow and evaporation are considered. For the sake of simplicity, rivulets are not explicitly considered in the present model. In the de-icing model, runback water flow and evaporation together with ice accretion and phase change within the ice layer are considered. Section III presents the explicit numerical approach used to solve the heat problem, and both homogeneous and multilayered composite substrates are considered. Details about the numerical integration of the runback water flow, ice accretion equations can be found in [9] and are omitted in this paper for the sake of conciseness. Various test results are presented in Sec. IV, where some comparisons with existing codes have also been provided as a validation exercise.

II. Governing Equations of the Runback Water Flow, Ice Accretion Model with Heating Sources

A. Flow Problem with Phase Change

Figure 1 shows a typical configuration of the runback water flow, ice accretion problem. Let u, v, w be the components of the velocity field in the water film in the (x, y, z) directions. Whenever indices are used, these are also denoted u_1, u_2, u_3 in the (x_1, x_2, x_3) directions, respectively. The water film is assumed to behave as an incompressible Newtonian fluid with stress components

$$T_{ij} = -p\delta_{ij} + \mu_w\left(\frac{\partial u_i}{\partial x_j} + \frac{\partial u_j}{\partial x_i}\right) \tag{1}$$

where p is the water pressure and δ_{ij} the Kronecker symbol. The second term on the right-hand side is the viscous stress, and μ_w denotes the water viscosity. The incompressibility constraint is expressed by

$$\nabla \cdot \mathbf{u} \equiv \frac{\partial u}{\partial x} + \frac{\partial v}{\partial y} + \frac{\partial w}{\partial z} = 0 \tag{2}$$

The ICECREMO model developed in [7] is derived from Navier–Stokes equations by using the fact that the aspect ratio of the flow
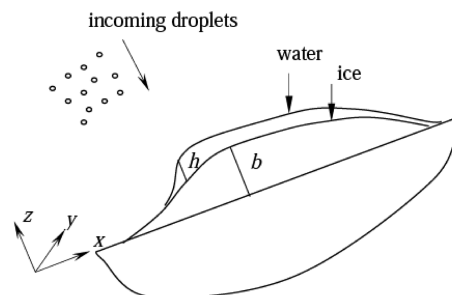

Fig. 1   Runback water flow/ice accretion model: problem geometry.

(depth scale over length scale) is small, and this allows major simplifications in the governing differential system. Indeed, within the frame of such an assumption, also known as the lubrication approximation, Navier–Stokes equations simplify to

$$\mu_w \frac{\partial^2 u}{\partial z^2} = \frac{\partial p}{\partial x} - \rho_w g_x + \mathcal{O}(\varepsilon^2, \varepsilon^2 Re) \qquad (3)$$

$$\mu_w \frac{\partial^2 v}{\partial z^2} = \frac{\partial p}{\partial y} - \rho_w g_y + \mathcal{O}(\varepsilon^2, \varepsilon^2 Re) \qquad (4)$$

$$0 = \frac{\partial p}{\partial z} - \rho_w g_z + \mathcal{O}(\varepsilon^2, \varepsilon^2 Re) \qquad (5)$$

At the water–ice interface, the velocity field in the water film must satisfy the no-slip condition:

$$u = v = 0 \quad \text{at } z = b \qquad (6)$$

The nonmaterial surfaces which coincide with the water–air interface and the water–ice interface are described by the functions ψ^{wa} and ψ^{wi}, respectively:

$$\psi^{\mathrm{wa}}(x, y, z, t) = z - b(x, y, z, t) - h(x, y, t) = 0 \qquad (7)$$

$$\psi^{\mathrm{wi}}(x, y, z, t) = z - b(x, y, z, t) = 0 \qquad (8)$$

where b and h are the ice and water heights, respectively. These geometric surfaces have the following properties:

Unit normal

$$\mathbf{n}^{\mathrm{wa}} = \frac{\nabla \psi^{\mathrm{wa}}}{\|\nabla \psi^{\mathrm{wa}}\|} = (-\partial(b+h)/\partial x, -\partial(b+h)/\partial y, 1)$$
$$\times \{1 + [\partial(b+h)/\partial x]^2 + [\partial(b+h)/\partial y]^2\}^{-\frac{1}{2}} \qquad (9)$$

$$\mathbf{n}^{\mathrm{wi}} = \frac{\nabla \psi^{\mathrm{wi}}}{\|\nabla \psi^{\mathrm{wi}}\|}$$
$$= (-\partial b/\partial x, -\partial b/\partial y, 1)[1 + (\partial b/\partial x)^2 + (\partial b/\partial y)^2]^{-\frac{1}{2}} \qquad (10)$$

Unit tangents (with main components in the x and y directions, respectively)

$$\mathbf{t}_x^{\mathrm{wa}} = (1, 0, \partial(b+h)/\partial x)\{1 + [\partial(b+h)/\partial x]^2\}^{-\frac{1}{2}} \qquad (11)$$

$$\mathbf{t}_y^{\mathrm{wa}} = (0, 1, \partial(b+h)/\partial y)\{1 + [\partial(b+h)/\partial y]^2\}^{-\frac{1}{2}} \qquad (12)$$

$$\mathbf{t}_x^{\mathrm{wi}} = (1, 0, \partial b/\partial x)[1 + (\partial b/\partial x)^2]^{-\frac{1}{2}} \qquad (13)$$

$$\mathbf{t}_y^{\mathrm{wi}} = (0, 1, \partial b/\partial y)[1 + (\partial b/\partial y)^2]^{-\frac{1}{2}} \qquad (14)$$

The two surfaces move with the normal velocities $\mathbf{u}^{\mathrm{wa}}$ and $\mathbf{u}^{\mathrm{wi}}$ such that

$$\frac{D^{\mathrm{wa}} \psi^{\mathrm{wa}}}{Dt} \equiv \frac{\partial \psi^{\mathrm{wa}}}{\partial t} + u^{\mathrm{wa}} \mathbf{n}^{\mathrm{wa}} \cdot \nabla \psi^{\mathrm{wa}} = 0$$
$$\frac{D^{\mathrm{wi}} \psi^{\mathrm{wi}}}{Dt} \equiv \frac{\partial \psi^{\mathrm{wi}}}{\partial t} + u^{\mathrm{wi}} \mathbf{n}^{\mathrm{wi}} \cdot \nabla \psi^{\mathrm{wi}} = 0 \qquad (15)$$

where D^{wa}/Dt and D^{wi}/Dt denote the convective derivatives following the motion of water–air and water–ice interface surfaces, respectively. The normal velocities can be obtained by combining the preceding equation with Eqs. (7–10), which yield

$$u^{\mathrm{wa}} = \frac{\partial(b+h)}{\partial t}\{1 + [\partial(b+h)/\partial x]^2 + [\partial(b+h)/\partial y]^2\}^{-\frac{1}{2}} \qquad (16)$$

$$u^{\mathrm{wi}} = \frac{\partial b}{\partial t}[1 + (\partial b/\partial x)^2 + (\partial b/\partial y)^2]^{-\frac{1}{2}} \qquad (17)$$

The mass balance at the water–ice interface ($z = b$) reads

$$\rho_w(\mathbf{u} \cdot \mathbf{n}^{\mathrm{wi}} - u^{\mathrm{wi}}) = -\rho_i u^{\mathrm{wi}}$$

Using Eqs. (6), (10), and (17), the preceding equation leads to

$$w = \left(1 - \frac{\rho_i}{\rho_w}\right) \frac{\partial b}{\partial t} \quad \text{at } (z = b) \qquad (18)$$

Let $\dot{m}^I = \rho_A(-\beta W \mathbf{e}_z \cdot \mathbf{n}^{\mathrm{wa}} - u^{\mathrm{wa}})$ be the rate of mass supply by impinging droplets, where ρ_A denotes the mass density of water droplets in the air, β is the collection efficiency, and W is the freestream velocity. Note that the impingement direction of water droplets is assumed vertical, so that their velocity has the opposite direction of the unit vector $\mathbf{e}_z$ which has same orientation as the z axis. We denote $\dot{m}^E$ to be the rate of mass loss due to evaporation. The mass balance at the water–air interface ($z = b + h$) reads

$$\rho_w(\mathbf{u} \cdot \mathbf{n}^{\mathrm{wa}} - u^{\mathrm{wa}}) = \dot{m}^I + \dot{m}^E \quad \text{or}$$
$$\rho_w(u^{\mathrm{wa}} - \mathbf{u} \cdot \mathbf{n}^{\mathrm{wa}}) = \rho_A(u^{\mathrm{wa}} + \beta W \mathbf{e}_z \cdot \mathbf{n}^{\mathrm{wa}}) - \dot{m}^E \qquad (19)$$

Development of Eq. (19), using Eqs. (9) and (16) and assuming $\rho_A/\rho_w \ll 1$, leads to

$$w = \frac{\partial(b+h)}{\partial t} + u\frac{\partial(b+h)}{\partial x} + v\frac{\partial(b+h)}{\partial y}$$
$$- \frac{1}{\rho_w}(J_w - \dot{m}^E\{1 + [\partial(b+h)/\partial x]^2 + [\partial(b+h)/\partial y]^2\}^{\frac{1}{2}})$$
$$(\text{at } z = b + h) \qquad (20)$$

where $J_w \equiv \rho_A \beta W$ is the mass flux of impinging water droplets. The rate of mass evaporation $\dot{m}^E$ is related to the evaporative heat flux Q_e by

$$\dot{m}^E = \frac{Q_e}{L_e} \qquad (21)$$

where L_e is the latent heat of evaporation.

The continuity of stress at the water–air interface reads (assuming summation over repeated indices)

$$T_{ij}n_j^{\mathrm{wa}} = -pn_i^{\mathrm{wa}} + \mu_w\left(\frac{\partial u_i}{\partial x_j} + \frac{\partial u_j}{\partial x_i}\right)n_j^{\mathrm{wa}}$$
$$= -p_a n_i^{\mathrm{wa}} + \sigma\kappa n_i^{\mathrm{wa}} + (\delta_{ij} - n_i^{\mathrm{wa}}n_j^{\mathrm{wa}})\frac{\partial\sigma}{\partial x_j} + A_i + \frac{(\dot{m}^E)^2}{\rho_v}n_i^{\mathrm{wa}} \qquad (22)$$

where σ is the surface tension, $\kappa = -\nabla \cdot \mathbf{n}^{\mathrm{wa}}$ is the mean curvature, and $\mathbf{A}$ is the shear stress due to constant air shear. The term $(\dot{m}^E)^2/\rho_v$ represents the recoil pressure of evaporation, and ρ_v is the vapor mass density. To the leading order of the lubrication approximation, the preceding stress condition leads to

$$n_i^{\mathrm{wa}}T_{ij}n_j^{\mathrm{wa}} = -p = -p_a + \sigma\kappa + \frac{(\dot{m}^E)^2}{\rho_v} + \mathcal{O}(\varepsilon^2) \qquad (23)$$

$$\left(t_x^{\mathrm{wa}}\right)_i T_{ij}n_j^{\mathrm{wa}} = \mu_w\frac{\partial u}{\partial z} + \mathcal{O}(\varepsilon^2) = \mathbf{t}_x^{\mathrm{wa}} \cdot \sigma + A_1 \qquad (24)$$

$$\left(t_y^{\mathrm{wa}}\right)_i T_{ij}n_j^{\mathrm{wa}} = \mu_w\frac{\partial v}{\partial z} + \mathcal{O}(\varepsilon^2) = \mathbf{t}_y^{\mathrm{wa}} \cdot \nabla\sigma + A_2 \qquad (25)$$

The contribution of surface tension gradient to shear stresses in Eqs. (24) and (25) is often referred to as Marangoni effect. Here, surface tension gradient is due to the dependence of surface tension on temperature, which is assumed linear

$$\sigma = \sigma_0 - \gamma\left(T_w^* - T_w^{\text{sat}}\right) \tag{26}$$

where $T_w^*(x, y, t) \equiv T_w(x, y, z = b + h, t)$ is the temperature at the surface of the water film, and T_w^{sat} is the saturation temperature (below which surface tension does not increase anymore and remains equal to σ_0). The constant γ is positive. The stress condition at the water–air interface ($z = b + h$) becomes

$$p - p_a = -\sigma\kappa - \frac{(\dot{m}^E)^2}{\rho_v} \tag{27}$$

$$\mu_w \frac{\partial u}{\partial z} = \mathbf{t}_x^{\text{wa}} \cdot \nabla\sigma + A_1 \tag{28}$$

$$\mu_w \frac{\partial v}{\partial z} = \mathbf{t}_y^{\text{wa}} \cdot \nabla\sigma + A_2 \tag{29}$$

The integration procedure for the field Eqs. (2–5) is similar to that in Myers et al. [7]. Integrating Eq. (5) subject to Eq. (27) yields

$$p - p_a = \rho_w g_z (z - h) - \sigma\kappa - \frac{(\dot{m}^E)^2}{\rho_v} \tag{30}$$

Integrating Eq. (3) with respect to z, taking into account Eqs. (6) and (28), yields

$$\mu_w u = \frac{1}{2}\left(\frac{\partial p}{\partial x} - \rho_w g_x\right)[z^2 - b^2 - 2(z - b)(b + h)] + A_1'(z - b) \tag{31}$$

In the same way, integrating Eq. (4) with respect to z, taking into account Eqs. (6) and (29), yields

$$\mu_w v = \frac{1}{2}\left(\frac{\partial p}{\partial y} - \rho_w g_y\right)[z^2 - b^2 - 2(z - b)(b + h)] + A_2'(z - b) \tag{32}$$

where

$$\begin{aligned} A_1' &\equiv A_1 + \mathbf{t}_x^{\text{wa}} \cdot \nabla\sigma = A_1 - \gamma\mathbf{t}_x^{\text{wa}} \cdot \nabla\theta|_{z=b+h} \\ A_2' &\equiv A_2 + \mathbf{t}_y^{\text{wa}} \cdot \nabla\sigma = A_2 - \gamma\mathbf{t}_y^{\text{wa}} \cdot \nabla\theta|_{z=b+h} \end{aligned} \tag{33}$$

Integrating the incompressibility constraint (2) across the film, and using Leibniz theorem and the mass conservations (18) and (20), yields

$$\frac{\partial h}{\partial t} + \text{div}\mathbf{Q}^w = \frac{1}{\rho_w}\left(J_w - \rho_i\frac{\partial b}{\partial t} - \dot{m}^E\{1 + [\partial(b + h)/\partial x]^2 + [\partial(b + h)/\partial y]^2\}^{\frac{1}{2}}\right) \tag{34}$$

where $\mathbf{Q}^w = (Q_1^w \quad Q_2^w)$ is the water flux,

$$Q_1^w = \int_0^h u\,dz$$

$$Q_2^w = \int_0^h v\,dz$$

and

$$\text{div}\,\mathbf{Q}^w \equiv \frac{\partial Q_1^w}{\partial x} + \frac{\partial Q_2^w}{\partial y}$$

Inserting Eqs. (31) and (32) into the definitions of Q_1^w and Q_2^w yields

$$\begin{aligned} Q_1^w &= -\frac{1}{3}\frac{h^3}{\mu_w}\left(\frac{\partial p}{\partial x} - \rho_w g_x\right) + \frac{h^2}{2\mu_w}A_1' \\ Q_2^w &= -\frac{1}{3}\frac{h^3}{\mu_w}\left(\frac{\partial p}{\partial y} - \rho_w g_y\right) + \frac{h^2}{2\mu_w}A_2' \end{aligned} \tag{35}$$

Equations (30–32) and (34) give, respectively, the water pressure, water velocities, and water height. However, these unknowns are coupled to the temperature fields in the substrate, ice layer, and water film through the rate of ice growth $\partial b/\partial t$, the rate of mass evaporation $\dot{m}^E$, and the dependence of surface tension on temperature. Therefore, we need to consider the heat problem to obtain all the unknowns.

B. Heat Problem

Temperatures in the substrate, ice layer, and water film are denoted T_s, T_i, and T_w, respectively. Heat conduction is governed by the following equations:

$$\rho_s c_s \frac{\partial T_s}{\partial t} + \nabla \cdot \mathbf{Q}_s = 0 \quad (\text{for } -t_s \leq z \leq 0) \tag{36}$$

$$\rho_i c_i \frac{\partial T_i}{\partial t} + \nabla \cdot \mathbf{Q}_i = 0 \quad (\text{for } 0 \leq z \leq b) \tag{37}$$

$$\rho_w c_w \frac{\partial T_w}{\partial t} + \nabla \cdot (\mathbf{Q}_w + \rho_w c_w T_w \mathbf{u}) = 0 \quad (\text{for } b \leq z \leq b + h) \tag{38}$$

where $\mathbf{Q}_s = -k_s \nabla T_s$, $\mathbf{Q}_i = -k_i \nabla T_i$, and $\mathbf{Q}_w = -k_w \nabla T_w$ are heat fluxes in the substrate, ice, and water, respectively, and k_s, k_i, and k_w are the respective heat conductivities. The specific heat is denoted as c_s, c_i, and c_w for the substrate, ice, and water, respectively.

The following boundary and interface conditions must be satisfied.

At the inner surface of the substrate

$$\mathbf{Q}_s \cdot \mathbf{n} = Q_0 \quad (\text{at } z = -t_s) \tag{39}$$

where Q_0 is a heat supply from a de-icing (or anti-icing) system. If convection with hot air is prescribed, Q_0 will have the form $Q_0 = h_c(T_s - T_0)$, where h_c is a known heat transfer coefficient and T_0 is the air temperature.

At the substrate–ice interface, both temperature and heat flux must remain continuous (obviously, the temperature gradient will be discontinuous because of the difference in heat conductivities in the substrate and ice):

$$T_s = T_i \quad \text{and} \quad \mathbf{Q}_s \cdot \mathbf{n} = \mathbf{Q}_i \cdot \mathbf{n} \quad (\text{at } z = 0) \tag{40}$$

At the ice–water interface (glaze ice), the temperature is continuous and equal to the freezing temperature, whereas the heat flux undergoes a discontinuity according to the Stefan condition (see Appendix A):

$$T_i = T_w = T_f \quad \text{and} \quad \mathbf{Q}_i \cdot \mathbf{n} - \mathbf{Q}_w \cdot \mathbf{n} = -\rho_i L_f \frac{\partial b}{\partial t} \quad [\text{at } z = b(t)] \tag{41}$$

where L_f is the latent heat of freezing. At the free surface of the water film (glaze ice or wet surface), the heat flux must satisfy the condition

$$\mathbf{Q}_w \cdot \mathbf{n} = (Q_c + Q_d + Q_e) - (Q_k + Q_a) \quad [\text{at } z = b(t) + h(t)] \tag{42}$$

where Q_c, Q_d, and Q_e correspond to the heat loss due to convection, cooling by supercooled droplets and evaporation, respectively. The terms Q_k and Q_a represent energy supply due to kinetic energy of

impinging droplets and aerodynamic heating, respectively (see Appendix B for the expressions of these energy terms).

In the case of rime ice, the evaporative heat loss Q_e must be replaced by heat loss due to ice sublimation Q_{subl}:

$$\mathbf{Q}_i \cdot \mathbf{n} = (Q_c + Q_d + Q_{subl}) - (Q_k + Q_a + Q_l) \quad [\text{at } z = b(t)] \tag{43}$$

Note that there is an additional heating source due to the latent heat Q_l released by the impinging droplets that freeze instantaneously.

In regions where the substrate surface is dry and not affected by droplet impingement, the following condition applies:

$$\mathbf{Q}_s \cdot \mathbf{n} = Q_c - Q_a \quad (\text{at } z = 0) \tag{44}$$

In general, the substrate consists of a multilayered composite with different properties for each layer and embedded heaters at interfaces between layers. In this case, conditions to be prescribed at interfaces between substrate layers are specified as follows.

Continuity of temperature and heat flux

$$T_s^- = T_s^+ \quad (\text{for } z = z_I, I = 1, \dots, NI) \tag{45}$$

$$Q_s^- = Q_s^+ \quad (\text{for } z = z_I, I = 1, \dots, NI) \tag{46}$$

where z_I is the position of the interface I, and NI is the total number of interfaces. In the case where a heater of power $2Q_H$ is present at the interface,

$$Q_s^- = Q_s^+ = Q_{cond} + Q_H \tag{47}$$

where Q_{cond} is the heat flux due to conduction.

C. Semi-Analytical Expression of the Temperature in the Water Film

A semi-analytical expression can be obtained for the temperature in the water film if we neglect both transient and convection terms in Eq. (38). Furthermore, due to the small thickness of the water film, we also neglect the lateral heat flux. Hence, Eq. (38) reduces to the one-dimensional pseudosteady-state equation

$$\frac{\partial^2 T_w}{\partial z^2} = 0 \tag{48}$$

In other words, conduction dominates the heat transfer in the water film, whereas convective effects are negligible. Temperature T_w in the water film has the expression

$$T_w(x, y, z, t) = T^*(x, y, t) - \frac{Q^*(x, y, t)}{k_w}[z - b(x, y, t)] \tag{49}$$

Dependence of water temperature on time is only due to the dependence on time of the temperature $T^*(x, y, t)$ and flux $Q^*(x, y, t)$ at the surface of substrate/ice. It is easy to check that expression (49) of the temperature T_w in the water film satisfies the continuity of both temperature and heat flux at the water–substrate/ice interface. Therefore, the boundary condition (42) applies directly to the surface of the medium underneath the water film (substrate or ice) and reads

$$Q^* = (Q_c + Q_d + Q_e) - (Q_k + Q_a) \quad [\text{at } z = b(t)] \tag{50}$$

III. Numerical Integration

In the following, we assume that temperature values in the substrate–ice–water system are used explicitly in the flow-ice accretion calculation procedure. Hence, the two solution procedures for the problems of heat conduction and film flow-ice accretion are uncoupled. Temperatures can be updated regularly at intervals of one or more time steps of the flow-ice accretion calculation. The existing numerical integration procedure implemented in ICECREMO2 can be found in [9], and the following sections will only consider the numerical approach for the thermal history.

Heat conduction in the substrate–ice–water is governed by Eqs. (36–38) and (49). Boundary conditions are expressed by Eqs. (39), (42), and (43), the substrate-ice interface condition by Eq. (40), and the Stefan condition by Eq. (41). In the case of a multilayered substrate with embedded heaters, the interface conditions (45–47) must be considered. We denote A_Q^s and A_Q^i as the boundaries of substrate and ice where heat flux is prescribed.

Time is discretized into time steps Δt, and the volumes occupied by the substrate and the ice layer are discretized into control volumes (or cells) ΔV^s and ΔV^i, respectively. The substrate cells are generated once for all before starting the time stepping procedure. The number of cells over the substrate thickness should be known. In the case of a multilayered substrate, the number of cells over the thickness of each layer needs to be specified. The ice mesh is updated at regular intervals of time and cells are added as the thickness of ice increases. In the following, we give a brief presentation of the explicit integration procedure.

Integrating Eq. (36) over the time step and the substrate control volume yields

$$\int_{t_n}^{t_{n+1}} \int_{\Delta V^s} \frac{\partial}{\partial t}(\rho_s c_s T_s) \, dV \, dt + \int_{t_n}^{t_{n+1}} \int_{\Delta V^s} \nabla \cdot \mathbf{Q}_s \, dV \, dt = 0 \tag{51}$$

where $t_n = n\Delta t$ and $t_{n+1} = t_n + \Delta t$.

Hence, integrating the first term on the left-hand side of Eq. (51) with respect to time and applying the divergence theorem to the second term yields

$$\int_{\Delta V^s} \left(\rho_s c_s T_s^{n+1} - \rho_s c_s T_s^n \right) dV + \int_{t_n}^{t_{n+1}} \int_{\Delta A^s} \mathbf{Q}_s \cdot \mathbf{dA} \, dt = 0 \tag{52}$$

where ΔA^s is the boundary of ΔV^s, $\mathbf{dA} \equiv dA\mathbf{n}$, and $\mathbf{n}$ denotes the outward unit normal to the boundary. We use the approximation

$$\int_{\Delta V^s} \rho_s c_s T_s \, dV \simeq \rho_s c_s T_{sc} \Delta V^s \tag{53}$$

where T_{sc} is the temperature at the cell centroid. The second term on the left-hand side of Eq. (52) is calculated as follows:

$$\int_{t_n}^{t_{n+1}} \int_{\Delta A^s} \mathbf{Q}_s \cdot \mathbf{dA} \cdot dt = \int_{t_n}^{t_{n+1}} \left[\sum_F \int_{\Delta A_F^s} \mathbf{Q}_s \cdot \mathbf{dA} \right] dt$$

$$\simeq \sum_F \int_{t_n}^{t_{n+1}} \mathbf{Q}_{sF} \cdot \Delta \mathbf{A}_F^s \, dt \tag{54}$$

where $\mathbf{Q}_{sF}$ is the flux value at the face centroid and the summation in Eq. (54) extends over all faces that belong to the boundary ΔA^s of the cell. Equation (52) becomes

$$\rho_s c_s \left(T_{sc}^{n+1} - T_{sc}^n \right) \Delta V^s + \sum_F \int_{t_n}^{t_{n+1}} \mathbf{Q}_{sF} \cdot \Delta \mathbf{A}_F^s \, dt = 0 \tag{55}$$

We assume that the flux $\mathbf{Q}_{sF}$ can be interpolated between values $\mathbf{Q}_{sF}^n$ and $\mathbf{Q}_{sF}^{n+1}$ at times t_n and $t_{n+1} = t_n + \Delta t$ as

$$\mathbf{Q}_{sF} = \varepsilon \mathbf{Q}_{sF}^{n+1} + (1 - \varepsilon) \mathbf{Q}_{sF}^n; \qquad 0 \leq \varepsilon \leq 1 \tag{56}$$

Selecting values of ε such as $\varepsilon = 1$ and $\varepsilon = \frac{1}{2}$ leads to well-known schemes: Euler, fully implicit, and Crank–Nicolson. In the following, we will adopt a fully explicit time integration scheme and will select $\varepsilon = 0$, so that $\mathbf{Q}_{sF} = \mathbf{Q}_{sF}^n$ for $t_n \leq t \leq t_{n+1}$, where $\mathbf{Q}_{sF}^n$ is the value of the flux at time t_n. Equation (55) becomes

$$\rho_s c_s \left(T_{sc}^{n+1} - T_{sc}^n \right) \Delta V^s + \Delta t \sum_F \mathbf{Q}_{sF}^n \cdot \Delta \mathbf{A}_F^s = 0 \tag{57}$$

To include boundary conditions in the preceding equation, we use the following notations: η_s denotes the set collecting all face indices for faces of the current cell that belong to the boundaries A_Q^s. Equation (57) is rewritten in the more explicit form, which shows boundary conditions

$$\rho_s c_s \left(T_{\text{sc}}^{n+1} - T_{\text{sc}}^n\right)\Delta V^s + \Delta t \sum_{F \notin \eta_s} \mathbf{Q}_{\text{sF}}^n \cdot \Delta \mathbf{A}_F^s$$

$$+ \Delta t \sum_{F \in \eta_s} \mathbf{Q}_{\text{sF}}^n \cdot \Delta \mathbf{A}_F^s = 0 \tag{58}$$

The integration scheme being explicit, temperature at time t_{n+1} is readily obtained using Eq. (58)

$$T_{\text{sc}}^{n+1} = T_{\text{sc}}^n - \frac{\Delta t}{\rho_s c_s \Delta V^s}\left[\sum_{F \notin \eta_s} \mathbf{Q}_{\text{sF}}^n \cdot \Delta \mathbf{A}_F^s + \sum_{F \in \eta_s} \mathbf{Q}_{\text{sF}}^n \cdot \Delta \mathbf{A}_F^s\right] \tag{59}$$

The same integration procedure is used to obtain the temperature in the ice layer. We obtain

$$T_{\text{ic}}^{n+1} = T_{\text{ic}}^n - \frac{\Delta t}{\rho_i c_i \Delta V^i}\left[\sum_{F \notin \eta_i} \mathbf{Q}_{\text{iF}}^n \cdot \Delta \mathbf{A}_F^i + \sum_{F \in \eta_i} \mathbf{Q}_{\text{iF}}^n \cdot \Delta \mathbf{A}_F^i\right] \tag{60}$$

A similar approach can be used to discretize the water film so that both transient and convective terms can be included (with an upwind treatment of the convective term). Temperature in the water film will be given by

$$T_{\text{wc}}^{n+1} = T_{\text{wc}}^n - \frac{\Delta t}{\rho_w c_w \Delta V^w}\left[\sum_{F \notin \eta_w}\left(\mathbf{Q}_{\text{wF}}^n + \rho_w c_w T_w^n \mathbf{u}^n\right).\Delta \mathbf{A}_F^w\right.$$

$$\left. + \sum_{F \in \eta_w}\left(\mathbf{Q}_{\text{wF}}^n + \rho_w c_w T_w^n \mathbf{u}^n\right).\Delta \mathbf{A}_F^w\right] \tag{61}$$

where η_w is the set collecting all face indices for cell faces where heat flux is prescribed. However, numerical tests have shown that discretization of the water film is too time consuming, and both transient and convective terms have little effect on the solution. It is therefore preferable to use the semi-analytical expression for temperature in the water given by Eq. (49) rather than the preceding expression.

Equations (59–61) involve the calculation of heat flux at cell centroid. The calculation procedure is detailed for the substrate mesh, the same approach being used for ice and water meshes. For faces that belong to the boundary where heat flux is prescribed ($F \in \eta_s$), the calculation is straightforward and gives

$$\sum_{F \in \eta_s} \mathbf{Q}_{\text{sF}}^n \cdot \Delta \mathbf{A}_F^s = \sum_{F \in \eta_s} Q_0(\mathbf{x}_F, t_n)\Delta A_F^s \tag{62}$$

where $\mathbf{x}_F$ is the coordinate vector of the face centroid. For faces where heat flux is unknown, the following procedure is used:

$$\mathbf{Q}_{\text{sF}}^n = -k_s (\nabla T_s)_F^n \tag{63}$$

where the temperature gradient $(\nabla T_s)_F^n$ at face centroid, at time t_n, is approximated as the mean value of the gradients at the left and right cell centroids $(\nabla T_s)_L^n$ and $(\nabla T_s)_R^n$, that is,

$$(\nabla T_s)_F^n = \tfrac{1}{2}\left[(\nabla T_s)_L^n + (\nabla T_s)_R^n\right] \tag{64}$$

The gradient at cell centroid is computed as follows. Using the gradient theorem, we have

$$\int_{\Delta V} \nabla T_s \, dV = \int_A T_s \, dA \simeq \Delta V(\nabla T_s)_c \tag{65}$$

where ΔV denotes the cell volume, A the boundary of the cell, and $(\nabla T_s)_c$ the temperature gradient at cell centroid. Hence,

$$(\nabla T_s)_c = \frac{1}{\Delta V}\int_A T_s \, d\mathbf{A} = \sum_F \int_{A_F} T_s \, d\mathbf{A}_F \simeq \frac{1}{\Delta V}\sum_F (T_s)_F \mathbf{A}_F \tag{66}$$

Taking into account the boundary conditions on faces where heat flux is prescribed, Eq. (66) leads to the following expression of the temperature gradient at cell centroid:

$$(\nabla T_s)_c = \frac{1}{\Delta V}\left(\sum_{F \notin \eta_s}(T_s)_F \mathbf{A}_F + \sum_{F \in \eta_s}(T_s)_F \mathbf{A}_F\right) \tag{67}$$

where $(T_s)_F$ is the temperature at the face centroid and is approximated as

$$(T_s)_F = \tfrac{1}{2}(T_{sL} + T_{sR}) \quad \text{for } F \notin \eta_s \tag{68}$$

$$(T_s)_F = T_{sL} \quad \text{for } F \in \eta_s \tag{69}$$

This procedure is no longer valid for faces that belong to interfaces between substrate layers of different material properties or between substrate and ice, or ice and water, as the temperature gradients are no longer continuous across these interfaces. In this case, the following approach is used to obtain the heat flux at the face centroid: Let L_1 and L_2 represent the domains occupied by two layers that belong to two different materials in the system substrate–ice–water (Fig. 2).

We denote T_f and Q_f as the temperature and heat flux at the interface and $\nabla^+ T_s$, $\nabla^- T_s$ the normal temperature gradients on the interface sides in layer L_1 and layer L_2, respectively $[\nabla T_s = (\nabla T_s) \cdot \mathbf{n}]$, so that we have

$$(T_s)_A = T_f + \nabla^+ \delta_A + \mathcal{O}(\delta_A)^2 \qquad (T_s)_B = T_f - \nabla^- \delta_B + \mathcal{O}(\delta_B)^2 \tag{70}$$

The jump in the temperature gradient satisfies the flux continuity:

$$Q_f = -K_1(\nabla^+ T_s) = -K_2(\nabla^- T_s) \tag{71}$$

Equations (70) and (71) yield

$$\nabla^+ T_s = \frac{K_B}{K_B \delta_A + K_A \delta_B}(T_A - T_B)$$

$$\nabla^- T_s = \frac{K_A}{K_B \delta_A + K_A \delta_B}(T_A - T_B) \tag{72}$$

and

$$Q_f = -\frac{K_A K_B}{K_B \delta_A + K_A \delta_B}(T_A - T_B) \tag{73}$$

which is the expression of the heat flux to be used when a given face of the cell boundary belongs to the interface between two different materials.

In the case where the two layers belong to a composite substrate, and if a heater of power $2Q_H$ is present at the interface, the total flux at the cell face is given by

$$Q_f^{\text{tot}} = Q_f + Q_H \tag{74}$$

Equation (60) for heat update in the ice layer is used only for temperature increments that do not involve phase change. Phase change occurs for each cell as a whole. The cell melts/freezes, at the melting/freezing temperature T_f, when the amount of gained/released latent heat is equal to the amount of latent heat needed for the phase change to take place. During the process of gaining/losing latent heat, the cell temperature is constant and equal to the melting/freezing temperature T_f (Fig. 3). Temperature update with phase change is performed as follows: Assume that there is enough heat to transform an ice cell from the state of ice at temperature $T_1 < T_f$ to
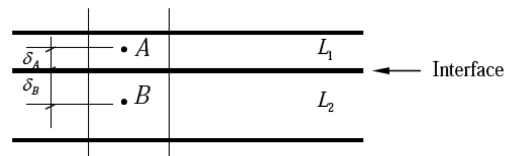

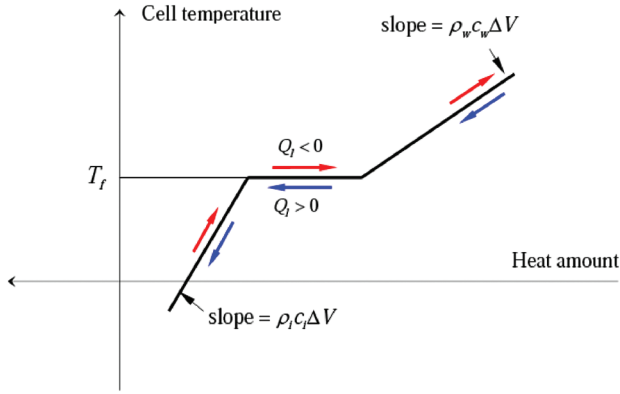Fig. 2 Interfaces between layers with different material properties.

Fig. 3   Cell temperature in the ice layer as a function of heat supply/release.

Fig. 4   Multilayered substrate for validation test case.

the state of water at temperature $T_2 > T_f$ during the heat update time step. The total heat supply to the cell is given by

$$\Delta Q = \Delta t \sum_F \mathbf{Q}_{iF} \cdot \mathbf{A}_F; \qquad (\Delta Q < 0) \qquad (75)$$

The energy required to rise the cell temperature to T_f is

$$Q_{\text{melt}} = -(T_f - T_1)\rho_i c_i V \qquad (76)$$

The energy absorbed as latent heat for the cell to melt is

$$Q_l = -\rho_i L_f V \qquad (77)$$

The new cell temperature is given by

$$T_2 = T_f + (Q_f - Q_{\text{melt}} - Q_l)/(\rho_w c_w V) \qquad (78)$$

IV.   Test Results

A.   Validation Test Cases

Results from a dry-air and a 2-D de-icing test case have been compared with data obtained with three different codes from the Defence Research Agency (DRA), NASA, and ONERA [10]. The problem geometry and main properties are shown on Fig. 4.

1.   Dry-Air Test Case

In this test case, the ice layer is ignored and the top surface is subject to a convective heat exchange with ambient air at temperature
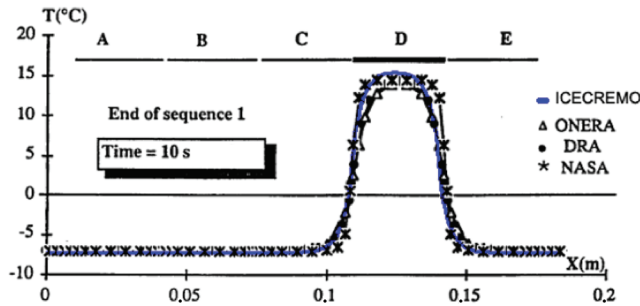
a)
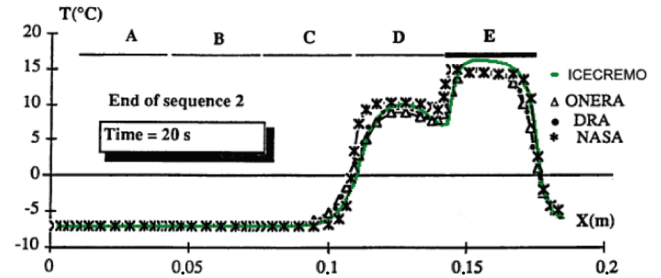
b)
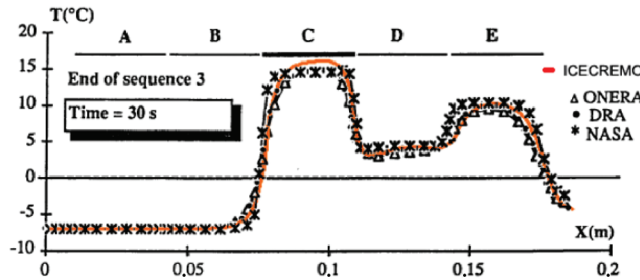
c)
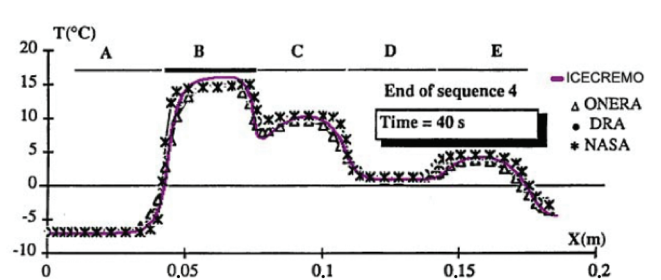
d)
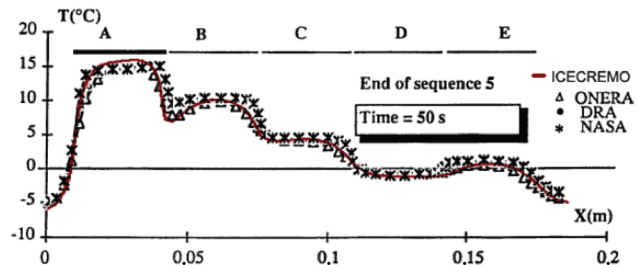
e)
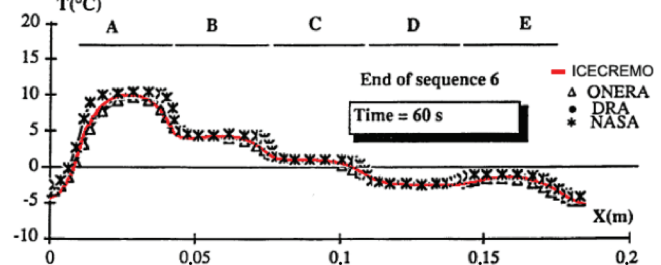
f)

Fig. 5   Dry-air test case: temperature at the top surface of substrate. Comparisons with data provided by DRA, NASA, and ONERA.

$-10°$C and a constant heat transfer coefficient of 300 W/m^2°C. Both lateral and bottom boundaries are assumed to be insulated. The heater elements have a power of 32 kW/m^2 each and are activated successively, in the sequence DECBA, each for a period of 10 s. The initial temperature of the substrate is assumed uniform and equal to $-7°$C.

Figure 5 shows surface temperature of the substrate at the end of each time interval during which a single heater is activated and at time 60 s where all heaters are switched off. The results are in good agreement with those of the three codes, which are shown on the same figure.

2. De-Icing Test Case

The geometry, layer properties, and boundary conditions are similar for this case to those of the dry-air test case. In the present case, an ice layer of 1.9 mm thickness is considered at the top surface of the substrate. The heat transfer coefficient at that surface is increased to 450 W/m^2°C to take into account ice roughness. The heater elements have the same power as in the previous case and are activated in the same sequence, DECBA.

Figure 6 shows temperature distribution at the ice–titanium interface at the end of each time interval, during which a single heater is activated and at time 60 s, when all heaters are switched off. A small difference in the maximum temperature is observed, but a discrepancy in the results provided by the three codes can also be noticed above the heated elements. This is probably due to the approach used in modeling phase change in the ice layer, which is not the same for all codes. ICECREMO2 considers melting at the level of each cell in the ice mesh. A cell is considered either completely frozen or completely melted.

Figure 7 shows the height of melted ice, which is in good agreement with the three codes. It is interesting to observe that above

the element *D*, for example, between 10 and 20 s elapsed time, the temperature decreases while the height of melted ice continues to increase. This is attributed to the significant amount of latent heat involved in the phase change, which causes the variation of the melted ice height to be much smaller than the variation in temperature. This phenomenon has been reproduced by all of the four codes. During the last 10 s, the melted ice begins to refreeze, which is caused by convective cooling at the surface, and this is also described by all of the four codes.

Figure 8 shows time history of the temperature at the ice–titanium interface in front of the center of each heater. Apart from the small difference in the maximum temperature, as explained earlier, all codes are in good agreement concerning the temperature history.

B. One-Dimensional Simulations of Anti-Icing

1. One-Dimensional Anti-Icing Simulation

A one-dimensional simulation of anti-icing has been performed on a horizontal flat plate of 0.5 m length. One row of 500×5 parallelepiped cells of 1 mm length, 1 mm thickness, and a time step of 0.001 s have been used. Droplets impinge perpendicularly to the plate. The collection efficiency and main data are shown in Fig. 9. The substrate inner surface is subject to a uniform heat supply from an anti-icing source.

Figure 10 shows the steady water height as a function of position on the surface for both unheated and heated cases with different values of the heat supply. At moderate heat supply amounts, the film has a linear shape outside the impingement region. For more significant heating and in the vicinity of the zone where full evaporation takes place, the film slope increases. These features, inherent to the water film evaporation, have also been observed in similar simulations by Al-Khalil et al. [3].
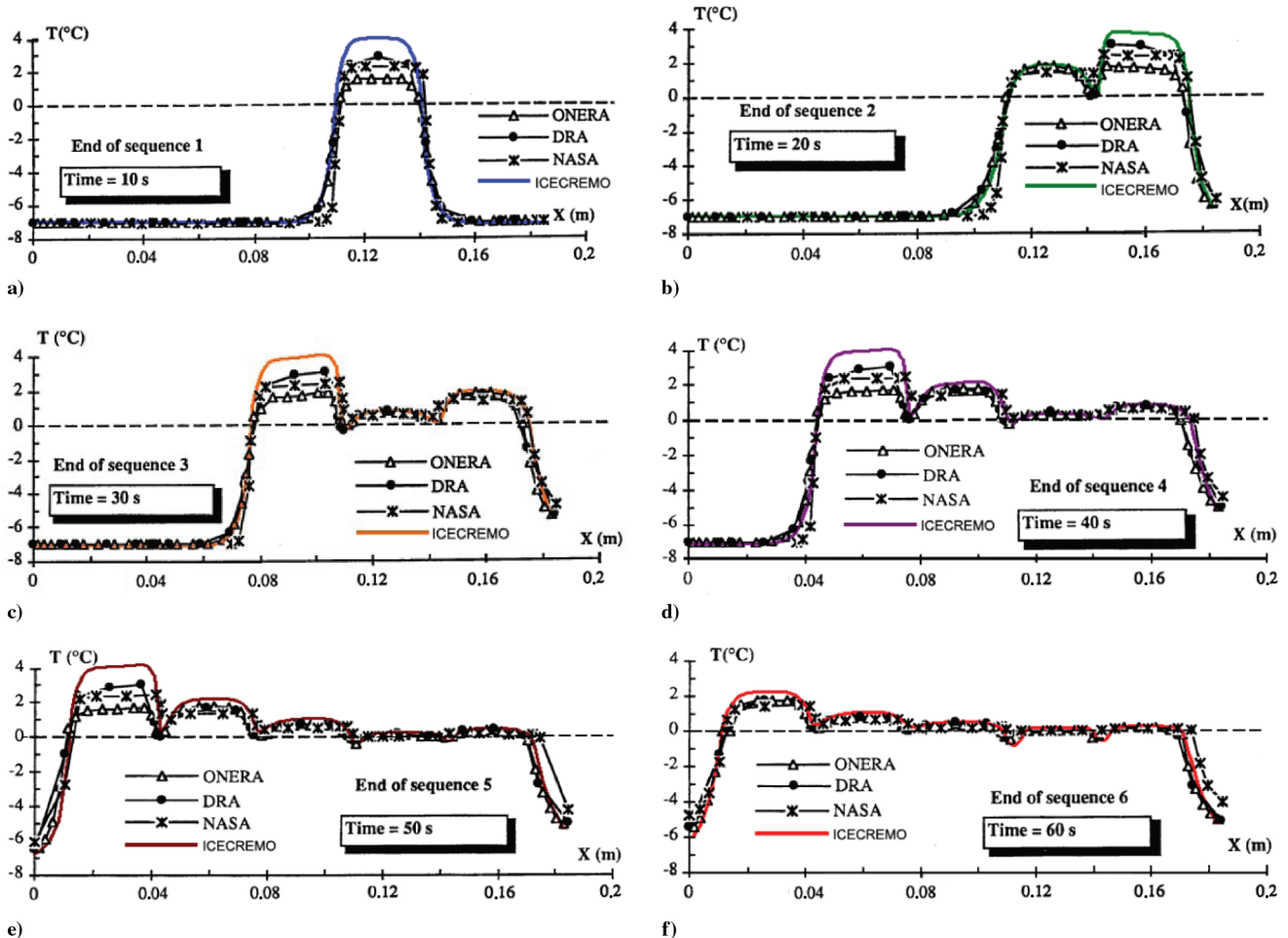

Fig. 6 De-icing test case: temperature at the ice–titanium interface. Comparisons with data provided by DRA, NASA, and ONERA.
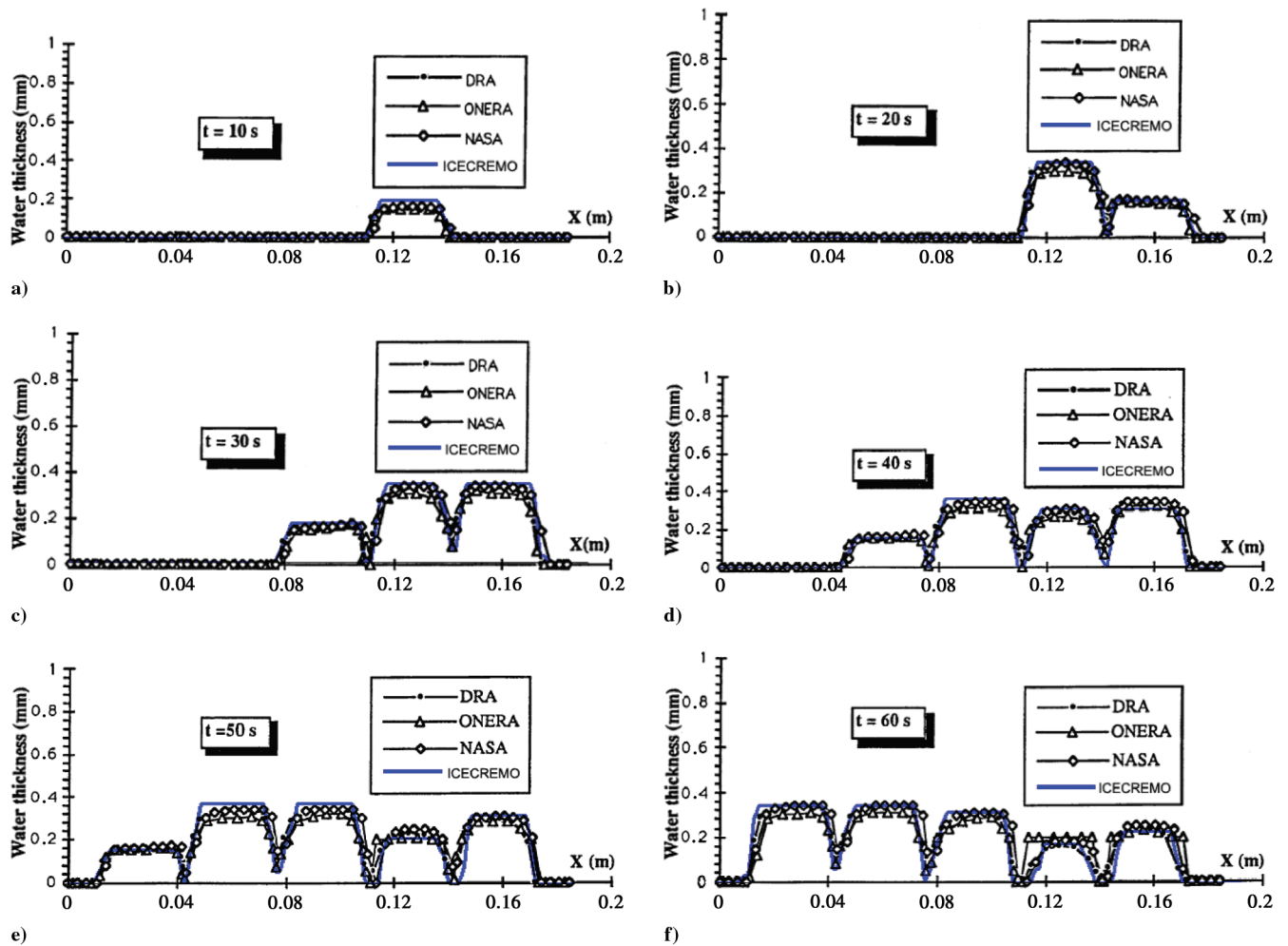
Fig. 7   De-icing test case: melted ice height. Comparisons with data provided by DRA, NASA, and ONERA.

Figure 11 shows the surface temperature once the steady state is established. Temperature on the left side, which is not affected by the droplet impingement, nor by the water film flow, is much higher than the temperature on the right side, where significant cooling due to water evaporation takes place.

Figures 12 and 13 show the temperature history at the locations M1 and M2, which are, respectively, within the impingement region and, at the right end, outside the impingement region. It can be observed that the rate of evaporation is much higher outside the impingement region and that full evaporation in that region would need a very high amount of heat. Therefore, anti-icing protection must extend sufficiently far from zones directly affected by droplet impingement to prevent runback water from freezing.

2.   One-Dimensional Anti-Icing Simulation Taking into Account Ice Accretion

The same data as in the previous simulation are used here. In the present simulation, ice accretion and melting of ice are considered. The ice layer is discretized using cells of 0.05 mm thickness. A uniform heat flux $Q = 10$ kW/m^2 is prescribed to the region of the substrate between $x = 0.05$ and 0.25 m. Figure 14 shows the ice shape in the unheated case (blue discontinuous line) after 2 min time.

The behavior under heating, after 2 min time, is shown on the same figure. Surface temperature (scale in Celsius on the right), freezing and melting fronts are also represented. It can be observed that the ice height obtained in the anti-icing case is well below the ice height obtained without heating the surface. Within the heated region and a close region outside, the freezing front coincides with the melting front, which means that the entire ice layer is melted. Melting outside of the heated zone occurs as a result of lateral conduction. Further on

the right, for $x > 0.3$ m, the ice heights are very close for both the unheated case and the anti-icing case. The melting front separates from the freezing front around $x = 0.32$ m. Beyond that position to the right, ice still forms, despite the heat supply. The melted ice height decreases gradually and disappears around $x = 0.32$ m.

Under the effect of the shear stress, which acts from left to right, the water film flows toward the right end and freezes over the region $x > 0.3$ m. The ice thickness in that region is comparable to that of the unheated case, and the amount of melted ice decreases as x increases and vanishes in the region where the temperature drops below zero.

C.   Three-Dimensional Simulations of Anti-Icing and De-Icing

1.   Three-Dimensional Anti-Icing Simulation

A three-dimensional simulation of anti-icing has been performed on a horizontal flat plate of 1 m length and 0.5 m width. A regular mesh of $100 \times 50 \times 5$ parallelepiped cells of 10 mm length and 1 mm thickness is used. The collection efficiency and main data are shown in Fig. 15.

Figure 16 shows the water film as it expands over the substrate surface and reaches the boundary under the effect of the shear stress, which acts in the x direction towards the right-hand side. In this case, there is no heat supply and the film shape shown at time $t = 30$ s corresponds to the steady flow.

Figure 17 shows a similar case with a uniform heat flux $Q_0 = 20$ kW/m^2 prescribed at the inner surface of the substrate. Comparing Figs. 16 and 17 at time $t = 30$ s, for example, clearly shows the effect of water evaporation on the film shape. The overall volume and shape of the water film are both affected by evaporation. The high amount of heat at the vicinity of the advancing front causes

the water film to become sharper as it evaporates. Surface temperature on the same figure shows the trace of the water film as a result of the coupling between heat conduction and water flow. Indeed, the zone affected by the water flow has a lower temperature, as the heat supply is uniform and the evaporative cooling adds to the cooling by convection in that region.
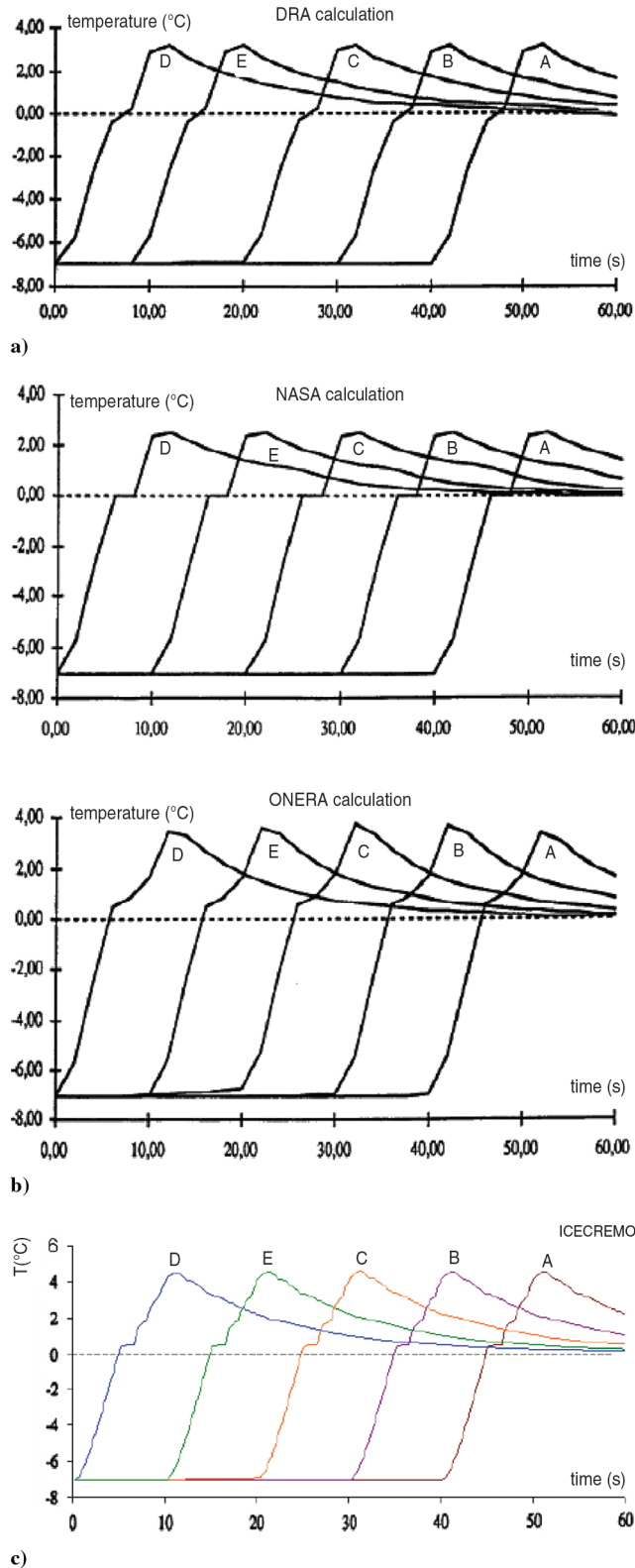

Fig. 8   De-icing test case: history of temperature at the ice/titanium interface, in front of the center of each resistance. Data provided by a) DRA, b) NASA and ONERA, and c) ICECREMO2.
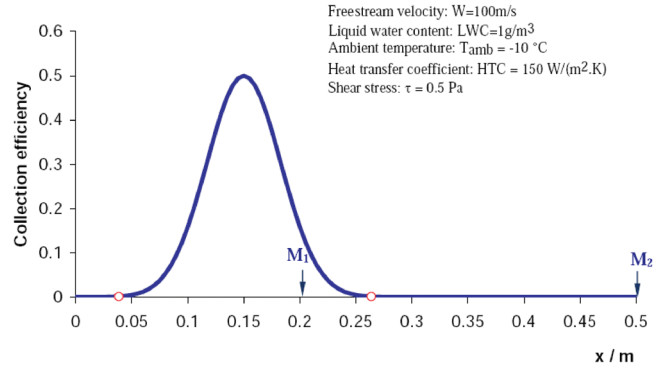
Fig. 9   One-dimensional simulation of anti-icing: collection efficiency and main data.
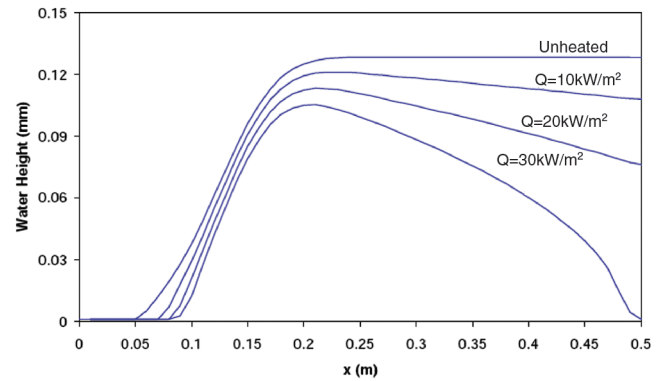
Fig. 10   One-dimensional simulation of anti-icing: steady water height.
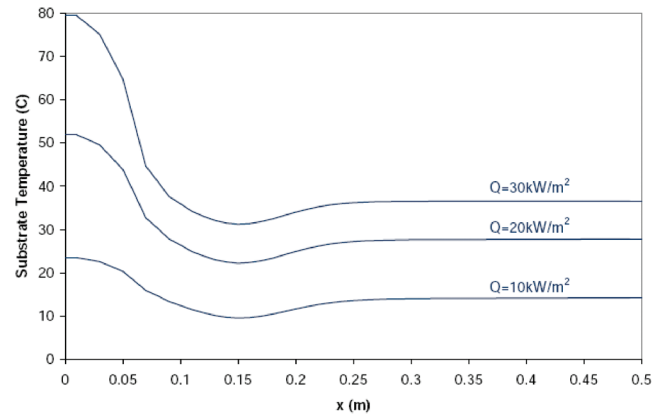
Fig. 11   One-dimensional simulation of anti-icing: surface temperature.
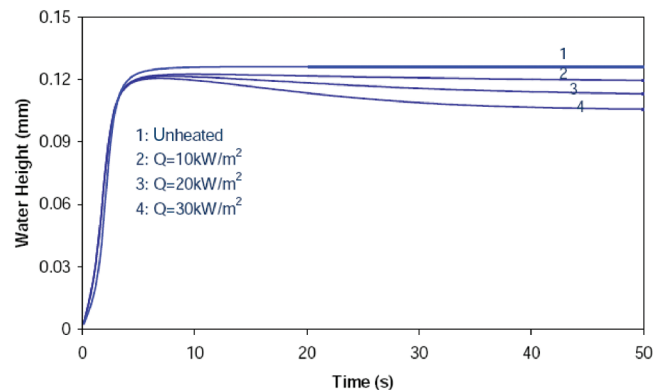
Fig. 12   One-dimensional simulation of anti-icing: water height history at location M_1.
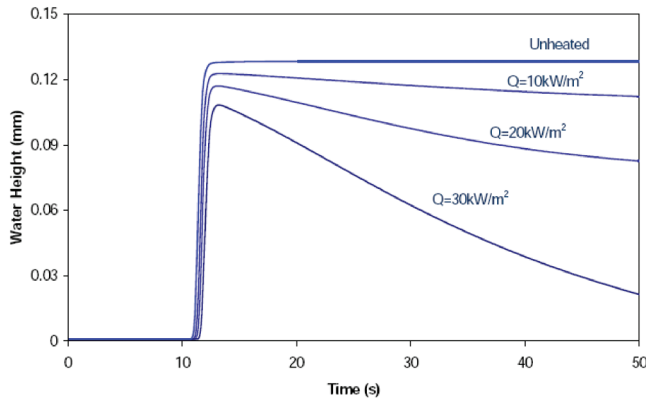
Fig. 13   One-dimensional simulation of anti-icing: water height history at location M_2.
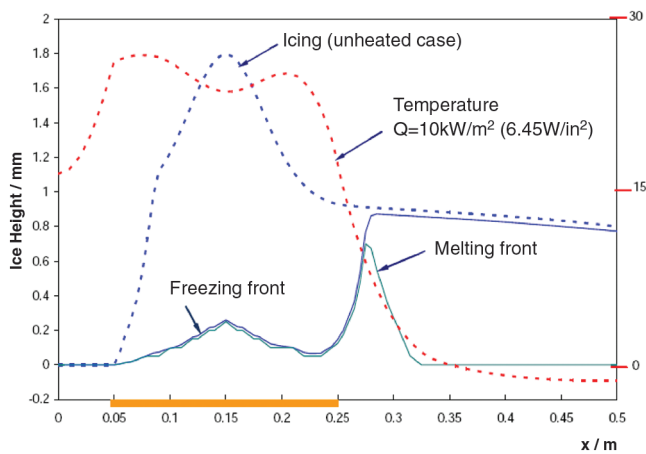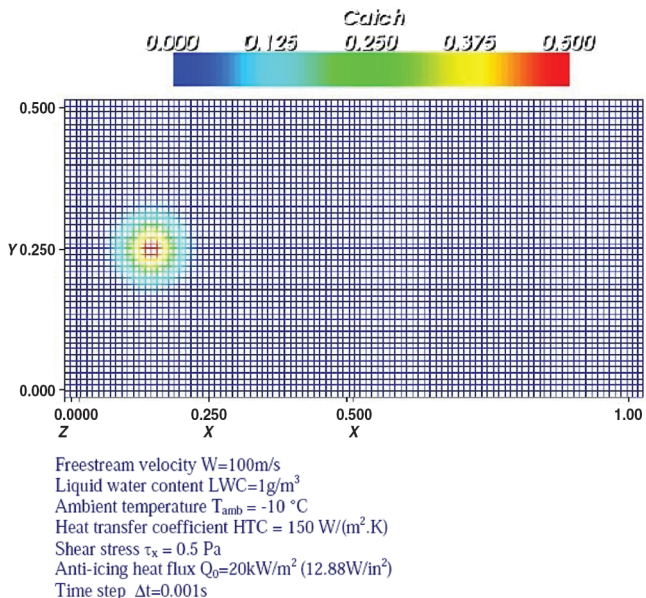

Fig. 14   One-dimensional simulation of anti-icing taking into account ice accretion: ice height and surface temperature.

2.   Three-Dimensional De-Icing Simulation

A three-dimensional simulation of de-icing has been performed on a flat square plate of 0.5 m side length. A regular mesh of $50 \times 50 \times 5$ parallelepiped cells of 10 mm length and 1 mm thickness is used. Collection efficiency and main data are shown in Fig. 18.

Freestream velocity W=100m/s
Liquid water content LWC=1g/m³
Ambient temperature T_{amb} = -10 °C
Heat transfer coefficient HTC = 150 W/(m².K)
Shear stress τ_x = 0.5 Pa
Anti-icing heat flux Q_0=20kW/m² (12.88W/in²)
Time step Δt=0.001s

Fig. 15   Three-dimensional simulation of anti-icing: collection efficiency and main data.
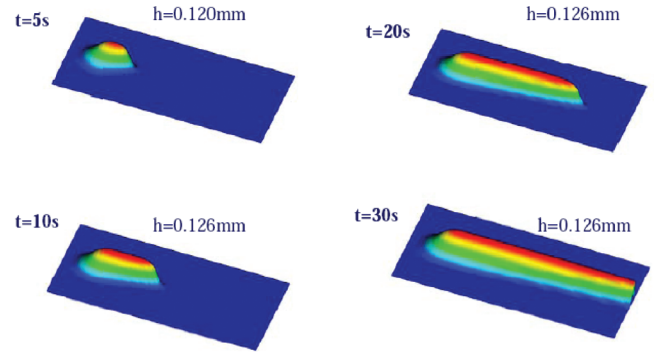

Fig. 16   Three-dimensional simulation of anti-icing: film flow on an unheated substrate.
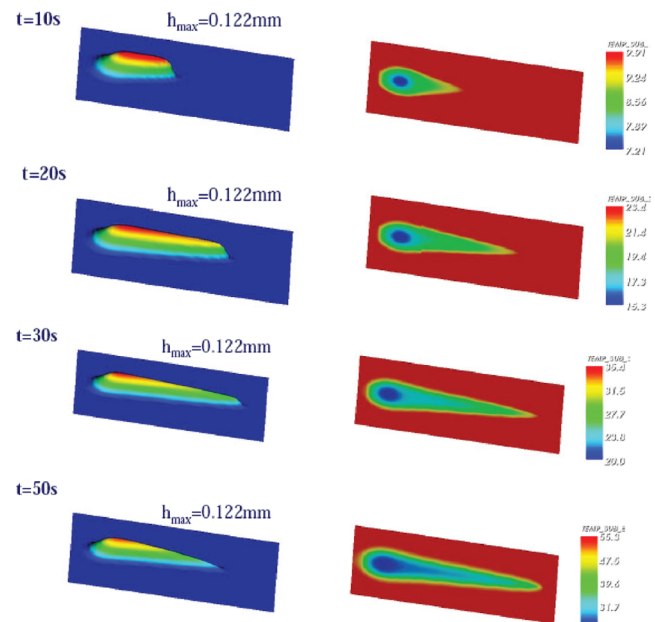

Fig. 17   Three-dimensional simulation of anti-icing: film flow and evaporation. Uniform heat flux $Q_0 = 20 \text{ kW/m}^2$.

A uniform heat flux $Q = G(t)Q_0$, where $G(t)$ is a time function shown in Fig. 19 and Q_0 has a constant value of 5 kW/m².

Figure 20 shows the surface temperature during the icing process at times $t = 120$ and 180 s. As in the case of the three-dimensional anti-icing simulation, Fig. 20 clearly shows the coupling between the three phenomena of film flow, ice accretion, and heat conduction. Indeed, the trace of the ice layer can be seen on the temperature pattern and slightly higher temperatures are observed within the zone affected by ice accretion. This phenomenon is observed when the heat supply is inactive, and the increase of temperature within the iced zone is due to the latent heat of freezing. However, in reality, due to the ice roughness, a higher heat transfer coefficient might be adequate at the ice surface and the larger convective cooling will influence the temperature distribution.

Figure 21 shows the surface temperature during de-icing at times $t = 210$ and 300 s. Now, it can be observed that temperature is much higher outside the zone affected by ice accretion. This is obviously due to the loss of energy in the form of latent heat that serves the phase change within the iced region.

Figure 22 shows the decrease in temperature after de-icing is switched off. At time $t = 480$ s, it can be observed that temperature is again higher inside the iced region, where refreezing at the surface of the melted ice might also take place.

Figures 23 and 24 show both ice and melted ice shapes during the de-icing process at times $t = 210$ and 300 s. It can be observed that, during the de-icing process, both ice accretion and melting of ice take
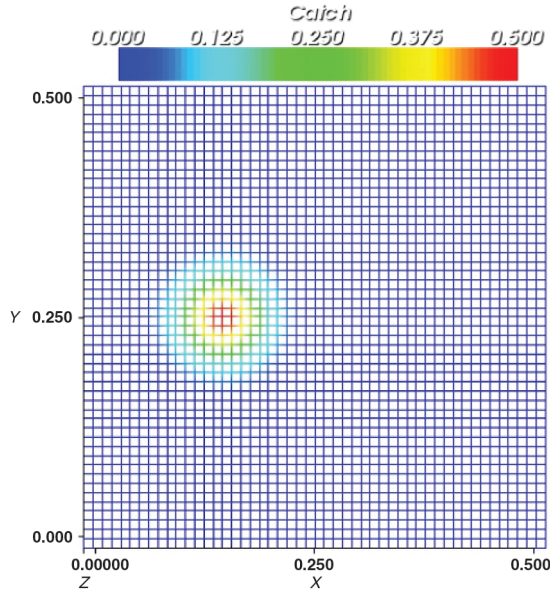
Freestream velocity W=100m/s
Liquid water content LWC=1g/m³
Ambient temperature T_{amb} = -10 °C
Heat transfer coefficient HTC = 150 W/(m².K)
Shear stress τ_x = 0.5 Pa
De-icing heat flux Q_0=5kW/m² (3.22W/in²)
Δz(ice)=0.05mm
Time step Δt=0.001s

Fig. 18 Three-dimensional simulation of de-icing: surface mesh and collection efficiency.

Fig. 20 Three-dimensional simulation of de-icing: substrate temperature during icing at $t = 120$ and 180 s.

Fig. 21 Three-dimensional simulation of de-icing: substrate temperature during de-icing at $t = 210$ and 300 s.

Fig. 22 Three-dimensional simulation of de-icing: substrate temperature during de-icing at $t = 360$ and 480 s.

place as long as temperature at the ice surface remains below freezing. However, in reality, a thin layer of melted ice will allow the ice to separate.

V. Conclusions

The runback water flow-ice accretion model developed by Myers et al. [7] and implemented in the 3-D icing code ICECREMO2 has been extended to consider anti-icing and de-icing situations. The new numerical tool uses an explicit finite volume approach that allows the film flow, ice accretion problem to be uncoupled from the heat conduction problem. This has resulted in producing an efficient numerical integration procedure that could be easily implemented in the transient icing code ICECREMO2. The numerical approach has been developed in such a way that it can handle both unstructured and structured grids and effectively extends the capabilities of ICECREMO2 to deal with anti-icing and de-icing calculations. Numerical experiments were first performed and compared with data provided by other icing codes to assess the validity of the present numerical procedure. Some simulations have also been performed in both one-dimensional and three-dimensional situations and were shown to capture the main features of anti-icing and de-icing processes.
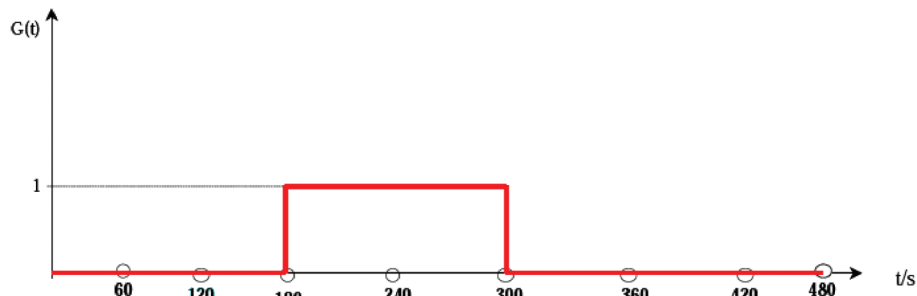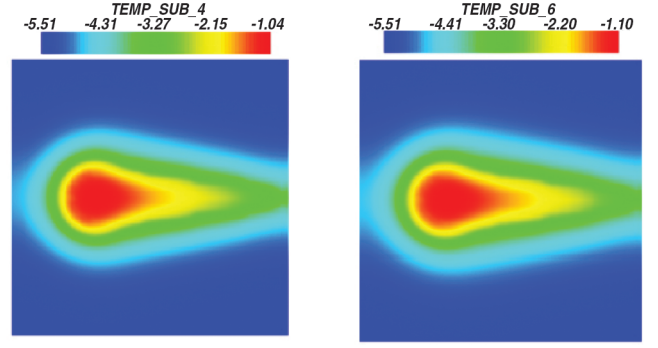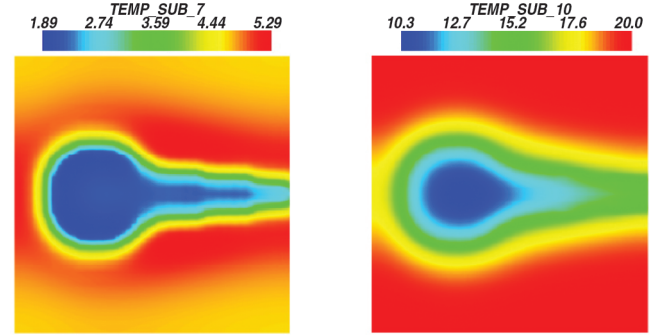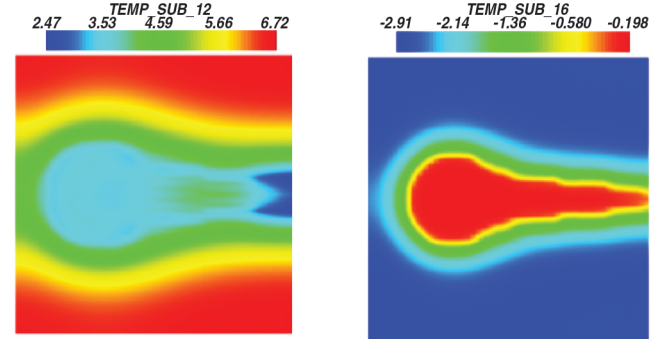
Appendix A: Stefan Condition

At the water-ice interface, we have a phase-change condition which is governed by the so-called Stefan energy balance equation or Stefan condition. As the freezing front moves a distance db during time dt, a quantity of heat $\rho_i L_F$ db is released from the water (liquid phase). Hence, during the time dt, we have $k_w (\partial T_w / \partial z)(b(t), t) \mathrm{d}t$
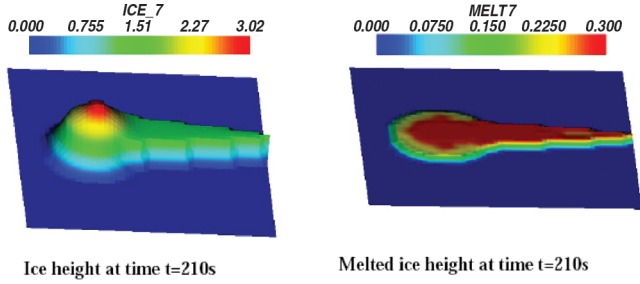

Fig. 19 Three-dimensional simulation of de-icing: time function for heat flux time variation.

Ice height at time t=210s   Melted ice height at time t=210s

Fig. 23 Three-dimensional simulation of de-icing: ice and melted ice heights (mm) at time t = 210 s.

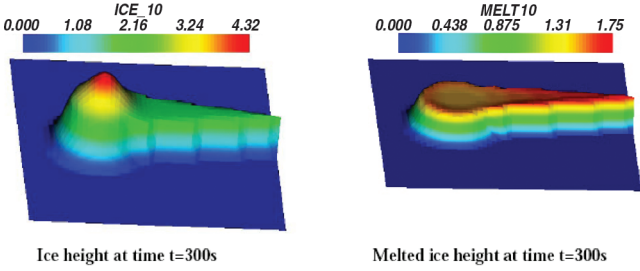Ice height at time t=300s   Melted ice height at time t=300s

Fig. 24 Three-dimensional simulation of de-icing: ice and melted ice heights (mm) at time t = 300 s.
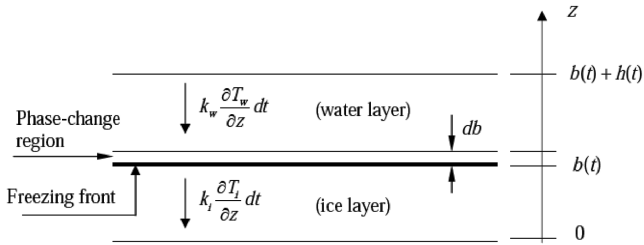

Fig. A1   Phase change at the freezing front.

units of heat flowing into the phase-change region from the water, as shown in Fig. A1, and $k_i(\partial T/\partial z)(b(t), t)\mathrm{d}t$ units of heat flowing out of the phase-change region into the ice. The difference must be equal to the released latent heat and we obtain

$$k_i \frac{\partial T}{\partial z} - k_w \frac{\partial T_w}{\partial z} = \rho_i L_F \frac{\partial b}{\partial t} \qquad (A1)$$

where L_F denotes the latent heat of freezing (in general, the latent heat of a given phase change is the quantity of heat released or absorbed when a unit of mass undergoes that phase change completely and isothermally). Equation (A1) shows that the freezing front moves in such a way that its velocity is proportional to the jump in the heat flux across the front (Fig. A1).

Appendix B: Expressions of Energy Terms Involved in Surface Heat Exchange

In the case of glaze ice, heat balance at the surface of the water film reads

$$\mathbf{Q}_w \cdot \mathbf{n} = (Q_c + Q_d + Q_e) - (Q_k + Q_a)$$

where Q_c, Q_d, and Q_e correspond to the heat loss due to convection, cooling by supercooled droplets, and evaporation, respectively. The

terms Q_k and Q_a represent energy supply due to kinetic energy of impinging droplets and aerodynamic heating, respectively. These terms have the expressions (see, for instance, [11])

$$Q_c = \bar{H}(T_w - T_a), \qquad Q_d = \rho_A \beta W c_w (T_w - T_a),$$

$$Q_e = \frac{0.622 \bar{H} L_v}{c_a P_T L_e^{2/3}} \left[e_w \left(\frac{T_T}{T_w}\right) \left(\frac{P_L}{P_T}\right)^{-1/\gamma} - R_h e_\infty \left(\frac{P_T}{P_\infty}\right) \right], \qquad (B1)$$

$$Q_k = \frac{1}{2}(\rho_A \beta W^3), \qquad Q_a = \frac{1}{2}\frac{r\bar{H}}{c_a}W^2$$

where $\bar{H}$ is the heat transfer coefficient, T_a is the air temperature and is assumed to be the same as the droplets temperature, c_a is the specific heat of air, and r is the recovery factor. In the expression of the evaporative heat loss Q_e, L_v represents the latent heat of vaporization, P is the static pressure, P_T is total pressure, R_h is the humidity factor, T_T is the total temperature in Kelvin, T_w is the water temperature, e is the water vapor pressure, and L_e is the Lewis number. The subscripts ∞ and L indicate freestream and local, respectively, and w indicates the water surface.

Heat balance at the surface of rime ice reads

$$\mathbf{Q}_i \cdot \mathbf{n} = (Q_c + Q_d + Q_{\mathrm{subl}}) - (Q_k + Q_a + Q_l) \quad [\text{at } z = b(t)]$$
$$(B2)$$

where Q_{subl} denotes heat loss due to ice sublimation and has an expression similar to that of Q_e, with the ice temperature T_i instead of the water temperature T_w, and ice vapor pressure instead of water vapor pressure.

References

[1] Hardy, J. K., "Protection of Aircraft Against Ice," Society of Manufacturing Engineers Rept. No. 3380, British Royal Aircraft Establishment, July 1946.

[2] Al-Khalil, K. M., Keith, T. G., De Witt, K. J., Nathman, J. K., and Dietrich, D. A., "Thermal Analysis of Engine Inlet Anti-Icing Systems," AIAA Paper 89-0759, Jan. 1989.

[3] Al-Khalil, K. M., Keith, T. G., and De Witt, K. J., "Development of an Anti-Icing Runback Model," AIAA Paper 90-0759, Jan. 1990.

[4] Hansman, R. J., and Turnock, S. R., "Investigation of Surface Water Behaviour During Glaze Ice Accretion," *Journal of Aircraft*, Vol. 26, No. 2, Feb. 1989, pp. 140–147.
doi:10.2514/3.45735

[5] Hansman, R. J., Yamaguchi, K., Berkowitz, K., and Potapczuk, M., "Modelling of Surface Roughness Effect on Glaze Ice Accretion," AIAA Paper 89-0734, Jan. 1989.

[6] Thomas, S. K., Cassoni, R. P., and MacArthur, C. D., "Aircraft Anti-Icing and De-Icing Techniques and Modeling," *Journal of Aircraft*, Vol. 33, No. 5, Sept. 1996, pp. 841–854.
doi:10.2514/3.47027

[7] Myers, T. G., Charpin, J. P. F., and Thompson, C. P., "Slowly Accreting Ice Due to Supercooled Water Impacting on a Cold Surface," *Physics of Fluids*, Vol. 14, No. 1, 2002, pp. 240–256.
doi:10.1063/1.1416186

[8] Myers, T. G., and Hammond, D. W., "Ice and Water Film Growth from Incoming Supercooled Droplets," *International Journal of Heat and Mass Transfer*, Vol. 42, No. 12, 1999, p. 2233.
doi:10.1016/S0017-9310(98)00237-3

[9] Press, A. J., and Standingford, D., "Icecremo II Software Design Methodology," BAE Systems, U.K., JS15066, Dec. 2003.

[10] "Part 3: Electrothermal De-Icing System Modeling," NASA/ONERA/ Defence Research Agency TR 2/7766 PN, June 1993.

[11] Gent, R. W., Dart, N. P., and Cansdale, J. T., "Aircraft Icing," *Philosophical Transactions of the Royal Society of London, Series A: Mathematical and Physical Sciences*, Vol. 358, No. 1776, 2000, pp. 2873–2911.
doi:10.1098/rsta.2000.0689